Journal of Rock Mechanics and Geotechnical Engineering 16 (2024) 4683–4696

Contents lists available at ScienceDirect

Journal of Rock Mechanics and Geotechnical Engineering

journal homepage: www.jrmge.cn

Full Length Article

Rectangular tunnel heading stability in three dimensions and its predictive machine learning models

Jim Shiau [a, *], Suraparb Keawsawasvong [b], Van Qui Lai [c, d], Thanachon Promwichai [b], Viroon Kamchoom [e], Rungkhun Banyong [b]

[a] School of Engineering, University of Southern Queensland, QLD, Toowoomba, 4350, Australia
[b] Department of Civil Engineering, Thammasat School of Engineering, Thammasat University, Klong Luang, Pathumthani, 12120, Thailand
[c] Faculty of Civil Engineering, Ho Chi Minh City University of Technology (HCMUT), Ho Chi Minh City, Viet Nam
[d] Vietnam National University Ho Chi Minh City (VNU-HCM), Ho Chi Minh City, Viet Nam
[e] Excellent Centre for Green and Sustainable Infrastructure, Department of Civil Engineering, School of Engineering, King Mongkut's Institute of Technology Ladkrabang (KMITL), Bangkok, Thailand

ARTICLE INFO

Article history:
Received 15 August 2023
Received in revised form
8 November 2023
Accepted 31 December 2023
Available online 1 May 2024

Keywords:
Wide rectangular tunnel
Finite element limit analysis (FELA)
Multivariate adaptive regression spline (MARS)
Three dimensions (3D)
Stability analysis

ABSTRACT

Tunnel heading stability in two dimensions (2D) has been extensively investigated by numerous scholars in the past decade. One significant limitation of 2D analysis is the absence of actual tunnel geometry modeling with a considerable degree of idealization. Nevertheless, it is possible to study the stability of tunnels in three dimensions (3D) with a rectangular shape using finite element limit analysis (FELA) and a nonlinear programming technique. This paper employs 3D FELA to generate rigorous solutions for stability numbers, failure mechanisms, and safety factors for rectangular-shaped tunnels. To further explore the usefulness of the produced results, multivariate adaptive regression spline (MARS) is used for machine learning of big dataset and development of design equations for practical design applications. The study should be of great benefit to tunnel design practices using the developed equations provided in the paper.

1. Introduction

To optimize the use of underground space for railway and mining applications, a variety of possible shapes for tunnel sections were considered in the majority of tunnel design projects. For example, the use of tunnel boring machine (TBM) has been prevalent over the past few decades, and it has been demonstrated to be a reliable and cost-effective method for constructing circular tunnels. However, underground excavation with a square or rectangular geometry was not commonly observed in the past owing to several limitations during the construction process. The application of rectangular tunnels in box culverts is becoming increasingly popular nowadays as they offer greater economic benefits and greater adaptability to shallow overburdens than conventional circular tunnels. However, very few studies on the stability assessment of rectangular tunnels have been reported in the literature, despite the substantial growth in their use in recent years.

Previous researchers have conducted studied on the stability of tunnels in cohesionless and frictional soil over the past few decades using circular sections (Mühlhaus, 1985; Leca and Dormieux, 1990; Chambon and Corté, 1994; Sahoo and Kumar, 2014). While Mühlhaus (1985) used the stress-based lower bound (LB) limit theorem, most of the researchers investigated tunnels in cohesionless soil using the kinematics-based upper bound (UB) limit theorem. With regard to the diverse shapes of tunnels, numerous studies have been conducted for drained and undrained soils. These include tunnels in circular shape (e.g. Sloan and Assadi, 1993; Shiau and Sams, 2019; Shiau and Keawsawasvong, 2022), elliptical shape (e.g. Shiau et al., 2021a), and square shape (e.g. Assadi and Sloan, 1991; Abbo et al., 2013; Wilson et al., 2013; Shiau and Keawsawasvong, 2022). Dutta and Bhattacharya (2021) also employed two-dimensional (2D) LB analysis to calculate support pressures for rectangular tunnels in cohesionless soil. With the improved limit analysis technique using adaptive meshing and

* Corresponding author.
E-mail address: jim.shiau@usq.edu.au (J. Shiau).
Peer review under responsibility of Institute of Rock and Soil Mechanics, Chinese Academy of Sciences.

https://doi.org/10.1016/j.jrmge.2023.12.035

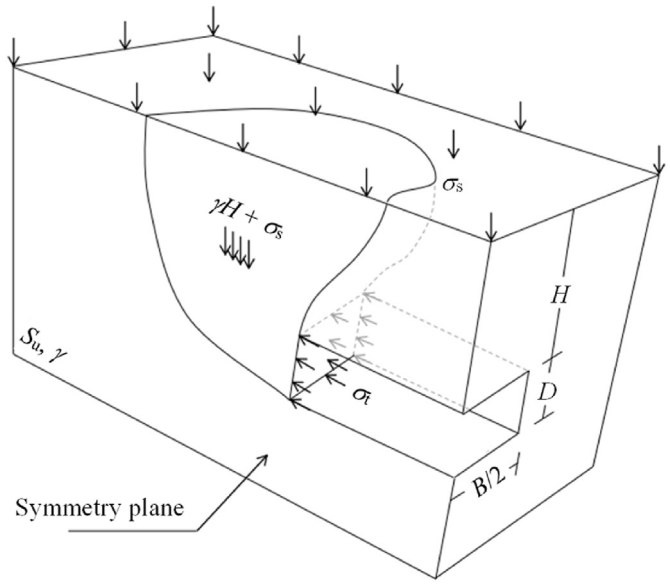

Fig. 1. Problem definition – 3D rectangular tunnel heading (1/2 domain).

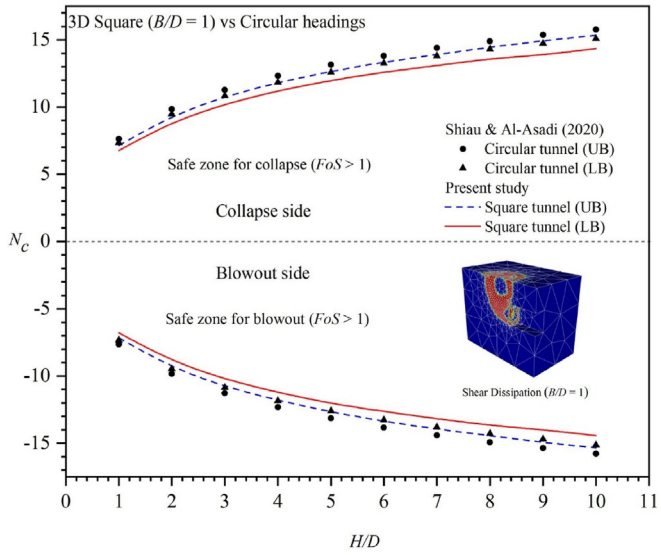

Fig. 3. The critical stability number N_c in collapse and blowout (3D rectangular vs. circular headings).

mathematical programming, Keawsawasvong and Ukritchon (2019), Shiau and Al-Asadi (2020), Shiau et al. (2021a, b), Keawsawasvong and Shiau (2022), and Shiau and Keawsawasvong (2022) also studied the stability of 2D circular tunnels and trapdoors. Meanwhile, Shiau and Al-Asadi (2018) revisited the problems by utilizing the original stability number stated in Broms and Bennermark (1967). Based on the 2D analysis of rectangular tunnels by Lai et al. (2023a), the patterns of rectangular tunnels are significantly different from those of circular tunnels. This is due to the fact that the failure zones of wide rectangular tunnels only occur at the corners of the tunnels.

Various three-dimensional (3D) tunnel face stability studies have been conducted in undrained conditions using the kinematic application of the limit theorems. Leca and Dormieux (1990) employed analytical UB analysis to determine the support pressure in cohesionless soil using a sliding cone failure mechanism. For cohesive and cohesionless soils, Mollon et al. (2010) improved UB solutions through the incorporation of various 3D failure mechanisms. Subsequently, Ukritchon et al. (2018) employed finite elements to examine the 3D undrained stability of a tunnel face in a heterogeneous clay, while Man et al. (2022) adopted the UB theorem for a rock mass face stability. In a recent study, Shiau and Al-Asadi (2020) used the 3D finite element limit analysis (FELA) approach to examine the stability of a circular tunnel heading in cohesive soil and obtained a series of 3D stability numbers, which can be used to estimate upper and LB tunneling pressures to prevent collapse.

Despite the above work, 3D analysis of rectangular tunnel face stability using FELA has never been investigated before. The objective of this study is to investigate the 3D undrained stability of rectangular tunnel headings in cohesive soils using FELA with an advanced adaptive meshing scheme. The present study employs a dimensionless stability number to express numerical findings from FELA, and then a multivariate adaptive regression spline (MARS) model is used for machine learning of big dataset and sensitivity analysis of each input parameter. The nonlinear relationships in the

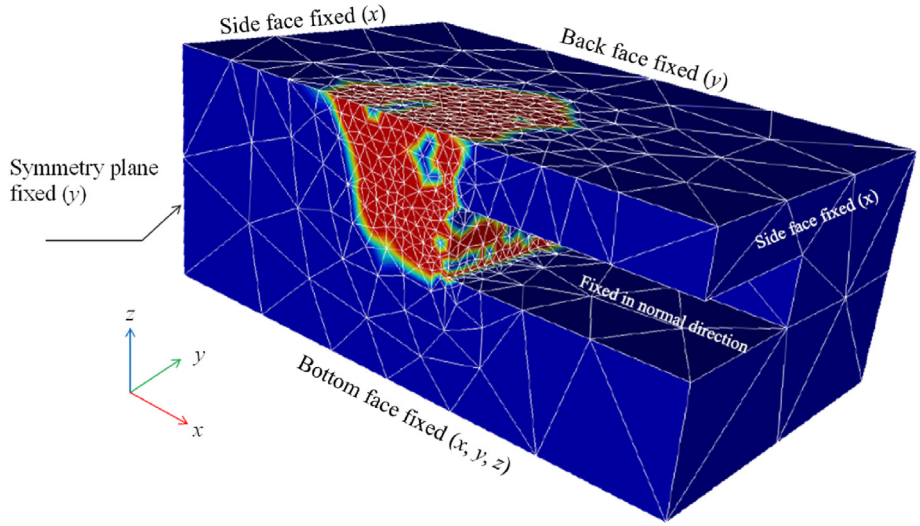

Fig. 2. A typical adaptive mesh (1/2 domain) and shear dissipation (H/D = 1, and B/D = 5).

Table 1
Comparison of N_c results in collapse – 3D square vs. circular headings.

H/D	Present study ($B/D = 1$)		Shiau and Al-Asadi (2020)	
	3D square, LB	3D square, UB	3D circular, LB	3D circular, UB
1	6.772	7.149	7.339	7.634
2	8.891	9.362	9.49	9.845
3	10.227	10.803	10.842	11.276
4	11.235	11.831	11.845	12.319
5	11.997	2.669	112.589	13.163
6	12.606	13.356	13.272	13.816
7	13.092	13.915	13.795	14.411
8	13.616	14.456	14.317	14.91
9	13.877	14.941	14.734	15.37
10	14.361	15.348	15.094	15.771

Table 2
Comparison of N_c results in blowout – 3D square vs. circular headings.

H/D	Present study ($B/D = 1$)		Shiau and Al-Asadi (2020)	
	3D square, LB	3D square, UB	3D circular, LB	3D circular, UB
1	−6.78	−7.152	−7.336	−7.641
2	−8.887	−9.373	−9.474	−9.843
3	−10.236	−10.792	−10.857	−11.286
4	−11.234	−11.809	−11.846	−12.314
5	−12.043	−12.68	−12.612	−13.15
6	−12.642	−13.378	−13.273	−13.843
7	−13.177	−13.949	−13.806	−14.41
8	−13.671	−14.43	−14.294	−14.931
9	−13.991	−14.944	−14.703	−15.361
10	−14.429	−15.34	−15.142	−15.774

input and output variables in several dimensions can be accurately captured using MARS. Several MARS-based design equations have been developed to predict stability numbers for the 3D rectangular tunnels, which offer more accurate and dependable stability assessments across the artificial set of data generated by FELA. This is of great benefit to tunnel designers in practice.

2. Problem statement

Fig. 1 presents the problem definition for a 3D rectangular tunnel heading under symmetrical condition. The rectangular tunnel is defined with a height of D, a width of B, and a soil cover of H. The soil surrounding the tunnel is considered to be homogeneous and isotropic, and it is assumed to be a perfectly rigid plastic material using the standard Tresca yield function, which is required by two strength parameters, namely the soil unit weight (γ) and the undrained shear strength (S_u). A uniform vertical surcharge pressure (σ_s) is applied to the ground surface in conjunction with the soil self-weigh, while a uniform internal pressure (σ_t) is applied to the face of the tunnel heading in order to support the overburden pressure.

The stability solution of a 3D rectangular tunnel heading can be represented using the critical stability number (N_c) approach proposed by Broms and Bennermark (1967) as well as those in Shiau and Al-Asadi (2020), who stated that the stability number is strongly related to several geometrical parameters. As demonstrated in Eq. (1), the cover-depth ratio (H/D) and the width-depth ratio (B/D) are incorporated.

$$N_c = \frac{\sigma_s + \gamma H - \sigma_t}{S_u} = f\left(\frac{H}{D}, \frac{B}{D}\right) \quad (1)$$

It should be noted that Eq. (1), which integrates the strength parameter $\gamma H/S_u$, can only be applied to the scenario of undrained analysis, as the influence of soil internal friction angle is negligible ($\phi = 0°$). The remaining variables in Eq. (1) are independent

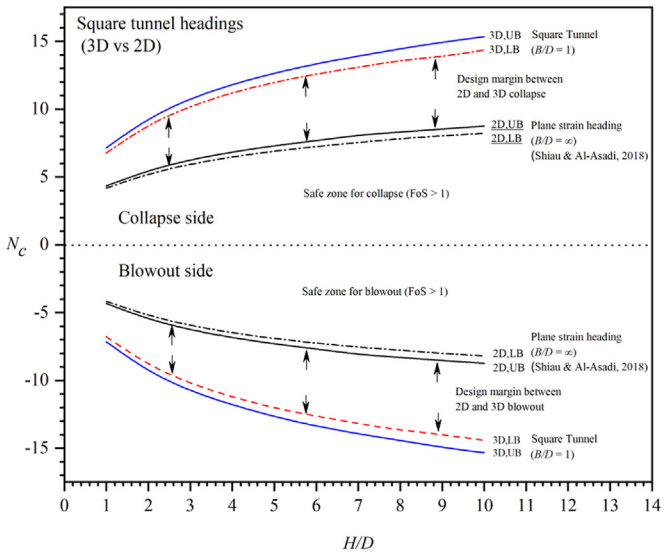

Fig. 4. Comparison of 2D and 3D N_c results ($FoS = 1$) in collapse and blowout.

Table 3
Comparison of N_c results in collapse – 3D square ($B/D = 1$) vs. 2D ($B/D = \infty$) plane-strain headings.

H/D	Present study ($B/D = 1$)		Shiau and Al-Asadi (2018) ($B/D = \infty$)	
	3D square, LB	3D square, UB	2D heading, LB	2D heading, UB
1	6.77	7.15	4.17	4.33
2	8.89	9.36	5.25	5.5
3	10.23	10.8	5.95	6.27
4	11.24	11.83	6.49	6.84
5	12	12.67	6.91	7.31
6	12.61	13.36	7.24	7.68
7	13.09	13.92	7.56	8.09
8	13.62	14.46	7.82	8.31
9	13.88	14.94	8.04	8.54
10	14.36	15.35	8.22	8.75

Table 4
Comparison of N_c results in blowout – 3D square ($B/D = 1$) vs. 2D ($B/D = \infty$) plane-strain headings.

H/D	Present study ($B/D = 1$)		Shiau and Al-Asadi (2018) ($B/D = \infty$)	
	3D square, LB	3D square, UB	2D heading, LB	2D heading, UB
1	06.78	07.15	04.16	04.33
2	08.89	09.37	05.24	05.5
3	010.24	010.79	05.94	06.27
4	011.23	011.81	06.5	06.85
5	012.04	012.68	06.91	07.31
6	012.64	013.38	07.26	07.68
7	013.18	013.95	07.55	08.09
8	013.67	014.43	07.76	08.3
9	013.99	014.94	08.01	08.54
10	014.43	015.34	08.19	08.74

constants, as N_c is the dimensionless critical stability number. In the present study, parametric analyses are performed using the selected practical design ranges such as H/D between 1 and 10 and B/D between 0.5 and 5. Given arbitrary constant values of σ_s, γ, and S_u, the objective function (i.e. the internal pressure σ_t) is to be optimized using nonlinear programming. Further details on achieving the solution are provided in the subsequent section.

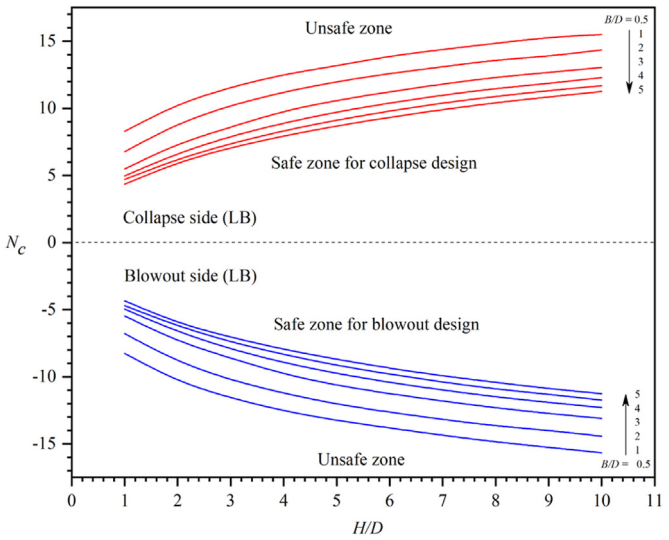

Fig. 5. 3D LB N_c result ($FoS = 1$) in collapse and blowout.

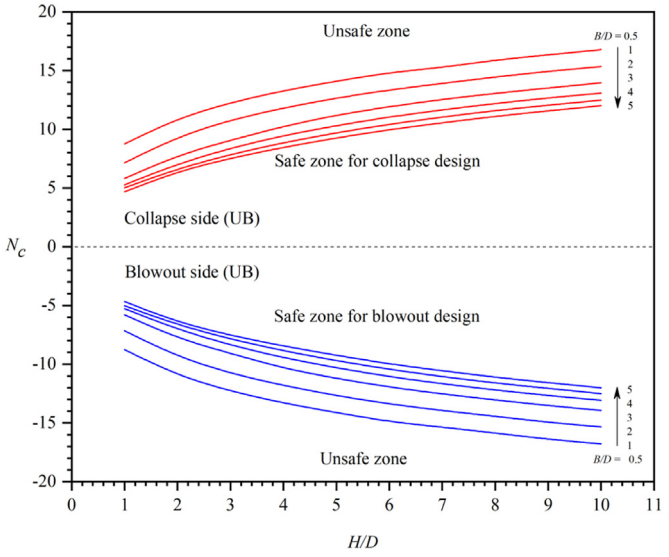

Fig. 6. 3D UB N_c result ($FoS = 1$) in collapse and blowout.

3. Method of analysis

This paper employs the latest 3D FELA code, OptumG3, to evaluate the soil stability of 3D rectangular tunnel headings in undrained clayey soils. The code was developed using the classic kinematic- and stress-based limit theorems, i.e. the UB and LB limit theorems. According to Sloan (2013), the lower bound finite elements method (FEM) is based on stress formulation in a nonlinear optimization problem. The element body forces and the nodal stresses are unknowns, and the objective function, which is to be maximized, corresponds to the collapse load. The unknown parameters are subjected to several constraints for each element, such as equilibrium equality, discontinuity equality, and a yield condition inequality constraint for each node. The upper bound FEM is derived from the kinematic formulation involved in a nonlinear optimization problem. Note that the nodal velocities, element stresses and plastic multipliers are the unknowns, the objective function, which is to be minimized, is the internal power dissipation minus the rate of work by fixed external forces in the classical UB method (Sloan, 2013).

Table 5
N_c results in collapse and blowout for 3D headings ($H/D = 1–5$).

H/D	B/D	N_c (collapse)		N_c (blowout)	
		LB	UB	LB	UB
1	0.5	8.285	8.763	−8.262	−8.775
	1	6.772	7.149	−6.78	−7.152
	2	5.475	5.805	−5.463	−5.8
	3	4.967	5.274	−4.963	−5.276
	4	4.701	5.022	−4.7	−5.032
	5	4.349	4.678	−4.334	−4.676
2	0.5	10.348	10.929	−10.364	−10.952
	1	8.891	9.362	−8.887	−9.373
	2	7.403	7.792	−7.37	−7.8
	3	6.653	7.051	−6.65	−7.042
	4	6.228	6.635	−6.22	−6.648
	5	5.98	6.411	−5.997	−6.413
3	0.5	11.588	12.277	−11.582	−12.297
	1	10.227	10.803	−10.236	−10.792
	2	8.6	9.063	−8.608	−9.075
	3	7.928	8.397	−7.935	−8.373
	4	7.390	7.862	−7.404	−7.862
	5	7.079	7.54	−7.055	−7.547
4	0.5	12.542	13.299	−12.544	−13.308
	1	11.235	11.831	−11.234	−11.809
	2	9.824	10.255	−9.804	−10.354
	3	8.918	9.474	−8.949	−9.459
	4	8.338	8.863	−8.339	−8.859
	5	7.951	8.467	−7.966	−8.459
5	0.5	13.17	14.104	−13.259	−14.113
	1	11.997	12.669	−12.043	−12.68
	2	10.596	11.218	−10.636	−11.209
	3	9.747	10.315	−9.756	−10.309
	4	9.143	9.717	−9.154	−9.715
	5	8.696	9.272	−8.696	−9.243

Table 6
N_c results in collapse and blowout for 3D headings ($H/D = 6–10$).

H/D	B/D	N_c (collapse)		N_c (blowout)	
		LB	UB	LB	UB
6	0.5	13.895	14.84	−13.814	−14.895
	1	12.606	13.356	−12.642	−13.378
	2	11.254	11.933	−11.261	−11.941
	3	10.403	11.058	−10.42	−11.055
	4	9.805	10.43	−9.806	−10.431
	5	9.353	9.975	−9.355	−9.982
7	0.5	14.388	15.27	−14.461	−15.349
	1	13.092	13.915	−13.177	−13.949
	2	11.803	12.549	−11.804	−12.528
	3	10.993	11.663	−10.682	−11.654
	4	10.405	11.043	−10.394	−11.056
	5	9.901	10.544	−9.936	−10.563
8	0.5	14.844	15.899	−14.851	−15.863
	1	13.616	14.456	−13.671	−14.43
	2	12.332	13.067	−12.311	−13.037
	3	11.49	12.2	−11.5	−12.191
	4	10.892	11.6	−10.913	−11.595
	5	10.424	11.104	−10.404	−11.098
9	0.5	15.302	16.34	−15.257	−16.39
	1	13.877	14.941	−13.991	−14.944
	2	12.673	13.528	−12.741	−13.51
	3	11.854	12.68	−11.908	−12.665
	4	11.329	12.057	−11.303	−12.058
	5	10.856	11.582	−10.888	−11.572
10	0.5	15.507	16.791	−15.671	−16.783
	1	14.361	15.348	−14.429	−15.34
	2	13.054	13.956	−13.102	−13.932
	3	12.296	13.085	−12.291	−13.068
	4	11.684	12.483	−11.737	−12.501
	5	11.261	12.01	−11.25	−12.002

The technique does not require the assumption of potential failure surfaces in advance, which contrasts with the analytical UB method and the traditional limit equilibrium method. In recent

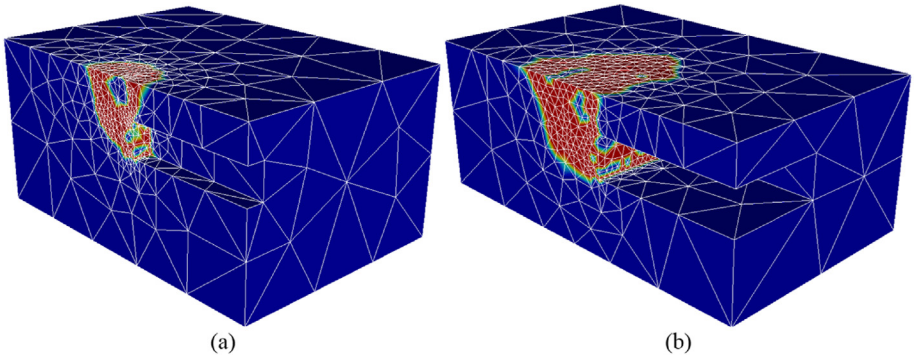

Fig. 7. Contour of shear dissipation showing potential failure mechanisms ($H/D = 1$): (a) $B/D = 1$; and (b) $B/D = 5$.

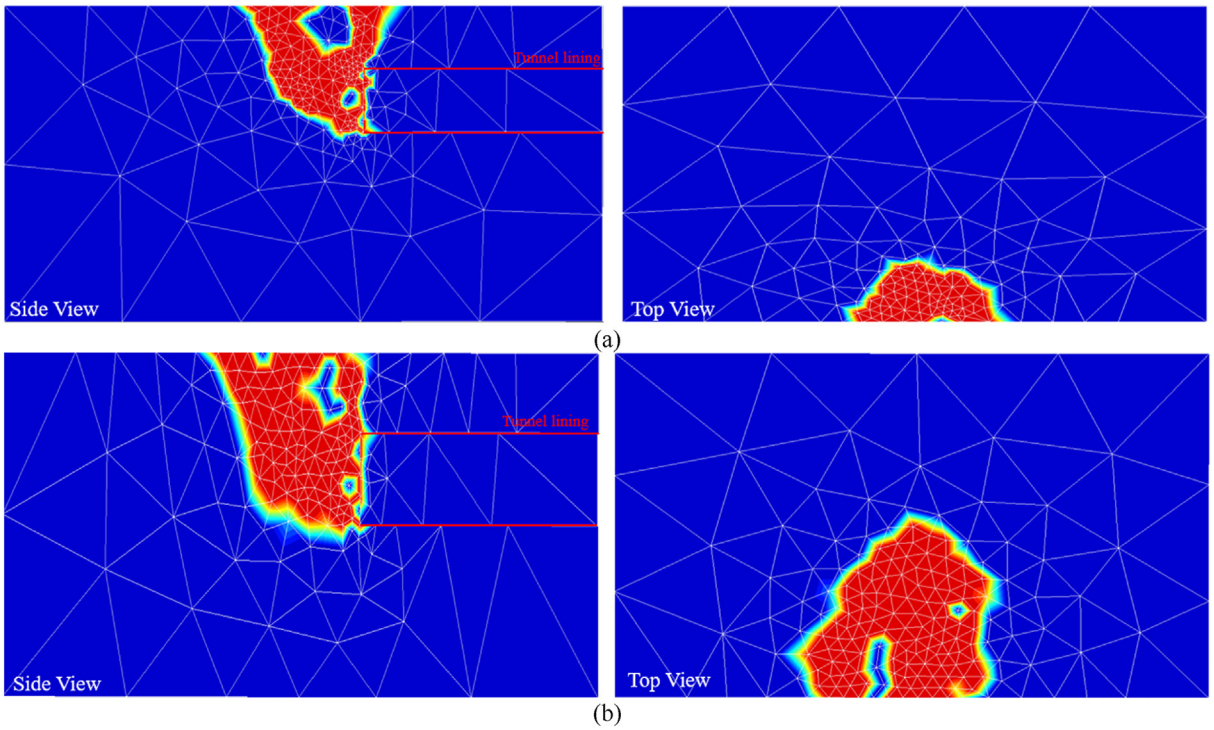

Fig. 8. Side and top views of shear dissipation contour ($H/D = 1$): (a) $B/D = 1$; and (b) $B/D = 5$.

years, the commercially available program has been widely used to study various soil stability problems with considerable success (OptumG3). The FELA theory differs from the traditional displacement-based finite element analysis, although both theories are based on the same concept of a discrete formulation.

Fig. 2 presents a typical numerical model using FELA. In every analysis, the adaptive meshing technique is employed to enhance the solution accuracy, as zones with large plastic shear strains would be given the highest mesh concentrations. This would enable the utilization of the boundary gap error estimator (OptumG3) to determine rigorous limit loads. In all studies presented, the adaptive meshing function was set to five iterations, with stepwise increases in the number of discretization elements from 5000 to 10,000. The averaged computation time was approximately 360 s for an i7-10610U CPU. Using this technique, the final adaptive mesh would resemble a colored plot of non-zero shear dissipations (see the colored contour in Fig. 2). It is important to note that the output values of the non-zero shear dissipations have no practical uses and are not typically included in technical reports on the study of perfectly plastic soil materials. Nevertheless, the key aspect of the shear dissipation plot, such as Fig. 2, is to show a potential failure mechanism. It is also important to note that the modeling size for the outer boundary is crucial because it ensures that the failure mechanism evolves naturally without any boundary effects. This has been subjected to rigorous testing to ensure the accuracy of the close UB and LB results presented in the paper.

The boundary conditions of the model are shown in Fig. 2. The two side faces are fixed in the x-direction, while the back face is limited to move only in the y-direction. For the symmetrical plane, all nodes are fixed in the y-direction (normal direction). The bottom boundary is set as a full constraint (i.e. fixed in x-, y-, and z-direction). The soil surface at the top and the inner tunnel surface are identified as free surfaces with movement in any direction. Given the input parameters comprising B, D, σ_s, γ, H, and S_u in both blowout and collapse calculations, the tunnel internal pressure (σ_t) is computed using OptumG3. The corresponding critical stability number N_c can then be calculated by substituting the computed σ_t into Eq. (1). It should be noted that this study examines both blowout (negative N_c) and collapse (positive N_c) situations. The numerical results of N_c are provided in the form of charts and

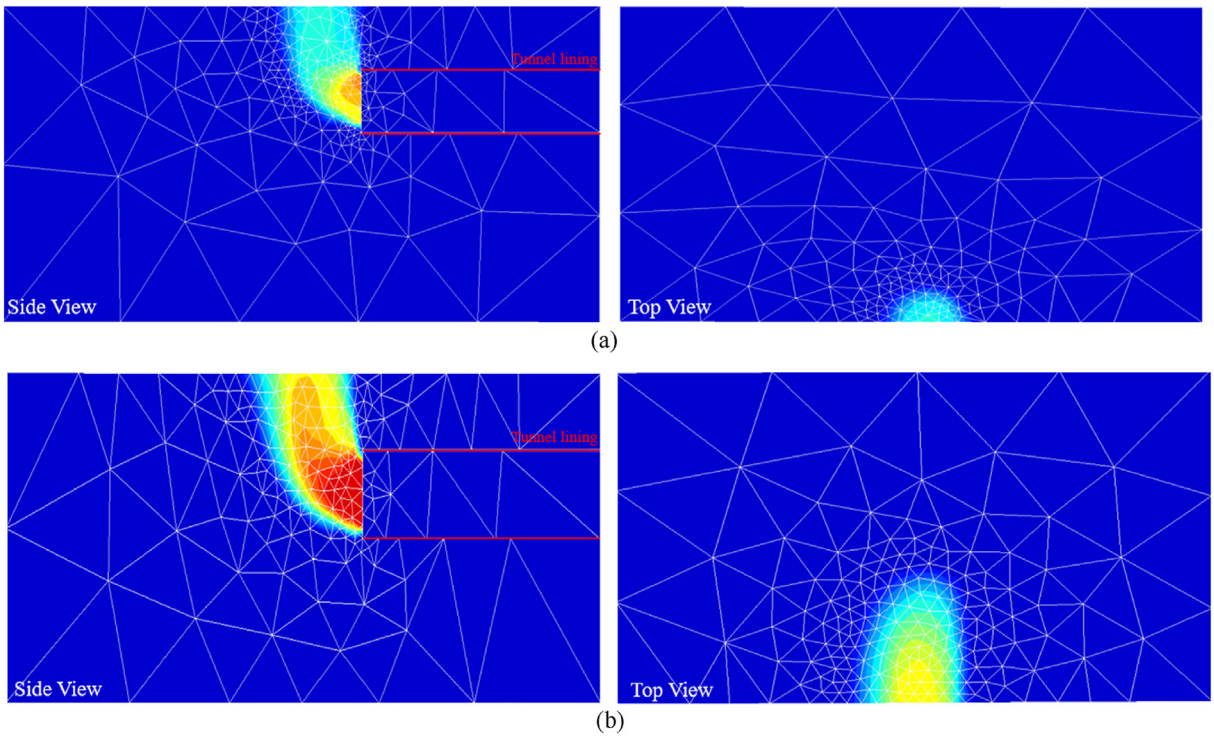

Fig. 9. Side and top views of velocity contour ($H/D = 1$): (a) $B/D = 1$; and (b) $B/D = 5$.

tables. Furthermore, the effects of several parameters on the developed failure mechanism are also presented using the total shear dissipation contour plot in this study.

4. Results and discussion

The numerical results of N_c for a 3D square tunnel heading ($B/D = 1$) are shown in Fig. 3 and Tables 1 and 2 for different depth ratios ($H/D = 1$–10). Both the UB and LB values of N_c are presented in collapse (positive N_c) and blowout (negative N_c) scenarios. On the collapse side (positive N_c), a nonlinearly increasing relationship between N_c and H/D is shown. The larger the H/D, the greater the N_c (i.e. the tunnel stability). It is noted that the N_c value fluctuates within 5% of the difference between UB and LB, and thus the current solutions are considered to be rigorous. They provide great confidence in producing all results in this paper.

In addition, the results of 3D square heading are compared to those of 3D circular heading (Shiau and Al-Asadi, 2020). The numerical results demonstrate that the results of the current square tunnel ($B/D = 1$) heading would yield a smaller N_c than those of 3D circular heading (with diameter D) by approximately 1%. It can therefore be concluded that the 3D circular tunnel heading is more stable than the square tunnel ($B/D = 1$). This is attributed to the geometrical arching effect, which is more pronounced in the circular tunnel in comparison to the square one. Interestingly, on the blowout side, N_c has the same magnitude but negative sign as that on the collapse side. By examining Eq. (1), it can be seen that a negative N_c value is only possible if the internal heading pressure σ_t is greater than the sum of σ_s and γH. This is a critical stability number, and the curves in Fig. 3 can be considered the failure

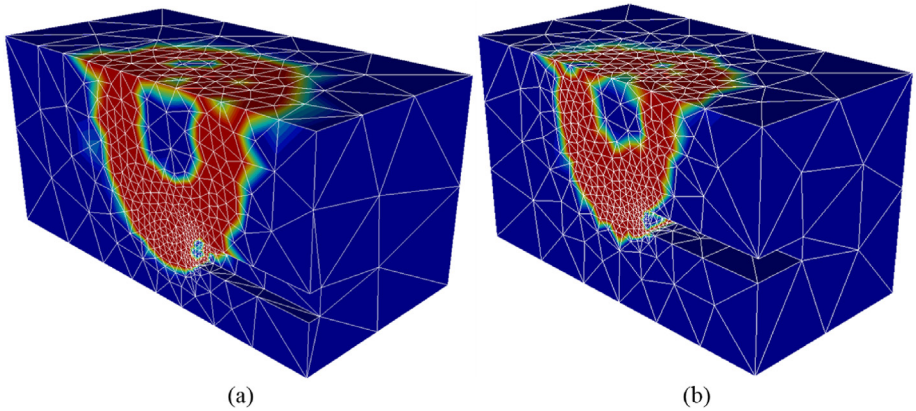

Fig. 10. Contour of shear dissipation showing potential failure mechanisms ($H/D = 5$): (a) $B/D = 1$; and (b) $B/D = 5$.

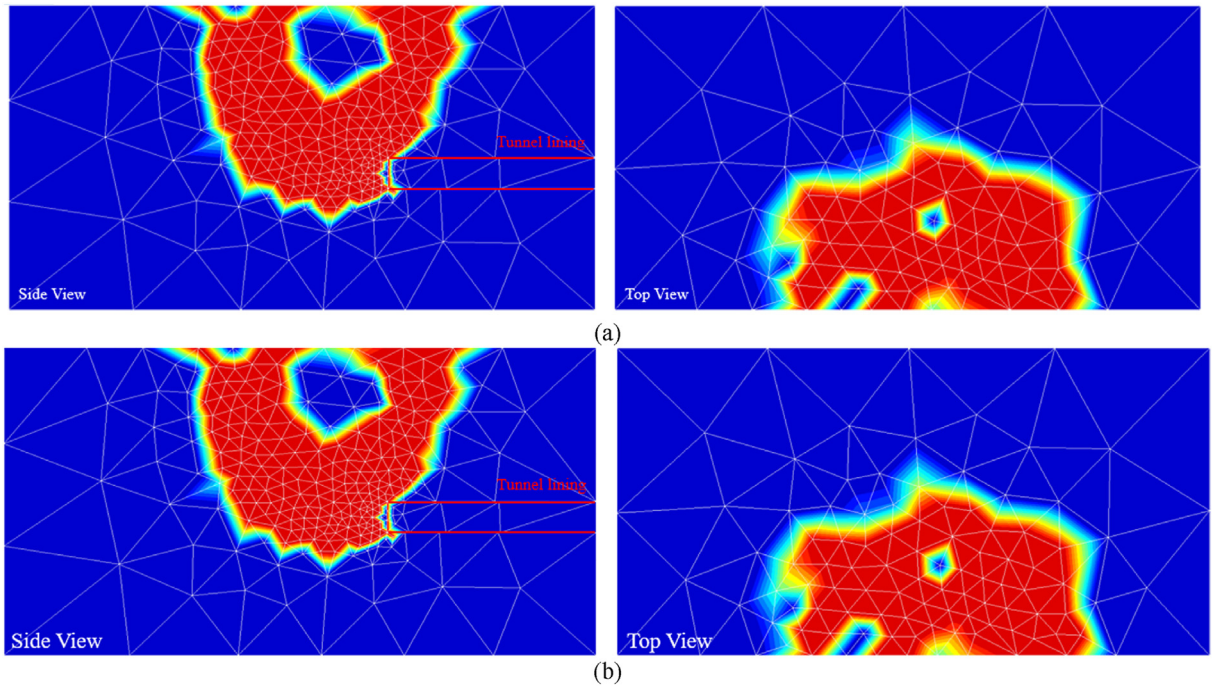

Fig. 11. Side and top views of shear dissipation contour ($H/D = 5$): (a) $B/D = 1$; and (b) $B/D = 5$.

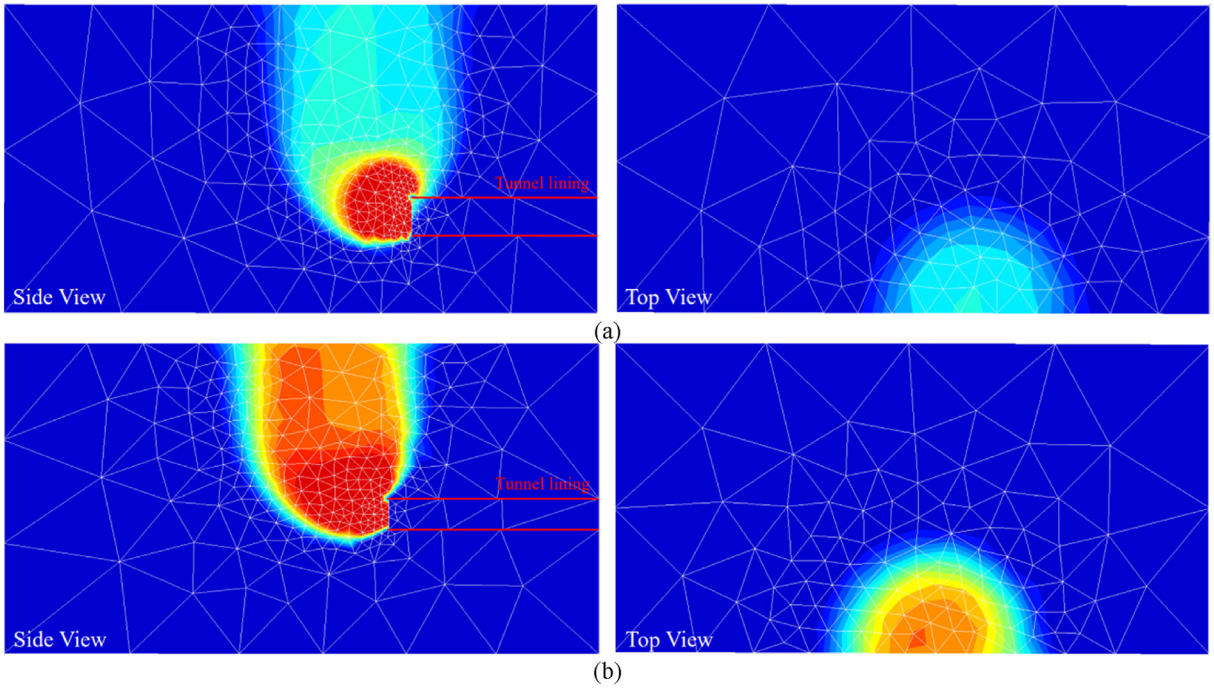

Fig. 12. Side and top views of velocity contour ($H/D = 5$): (a) $B/D = 1$; and (b) $B/D = 5$.

envelope. It is therefore advisable not to design a N_c value that is outside this envelope, as the factor of safety (FoS) would be less than one. Further discussion on the FoS will be presented in a later section.

The results of N_c for 3D square heading are further compared to those for 2D plane-strain headings ($B/D = \infty$) reported by Shiau and Al-Asadi (2018) for both the blowout and collapse scenarios, as shown in Fig. 4 and Tables 3 and 4, where the presented design margin between 2D and 3D analyses would greatly assist the designers in making decisions towards their final design. In general, the 3D analysis predicts larger values of N_c by approximately 1.7–1.9 times, depending on the value of H/D. Indeed, the 2D analysis would always result in conservative values of N_c, as it provides smaller values of N_c for design. As previously discussed, the blowout curves are simply a mirror image of the collapse curves, and their N_c values are now in negative sign. On the other hand, the discrepancy between the 2D and 3D results (the design margin shown in Fig. 4) would have indicated the necessity for

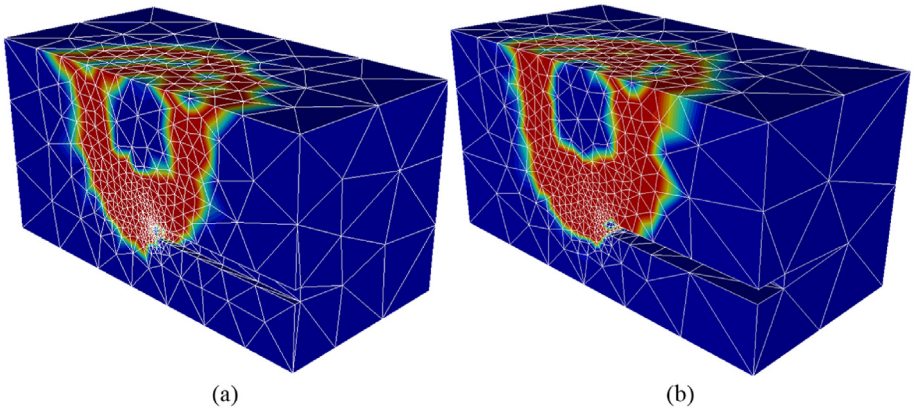

Fig. 13. Contour of shear dissipation showing potential failure mechanisms ($H/D = 10$): (a) $B/D = 1$; and (b) $B/D = 5$.

further investigation into the effects of 3D rectangular tunnel heading, particularly in cases where $B/D > 1$. This is discussed in more details in Figs. 5 and 6.

A comprehensive design chart of LB N_c values for 3D rectangular tunnels ($B/D = 0.5–5$) is presented in Fig. 5 for both collapse and blowout scenarios. It is noted N_c decreases as B/D increases. As discussed before, these curves represent the so-called failure envelope, beyond which the design is considered as unsafe. It is therefore important to ensure that the design value of stability number N_c is well within the envelope. For the sake of completeness, the UB results are presented in Fig. 6. However, in practice, the LB N_c results are normally adopted for design because they are conservative. It should be noted that the differences between the two bounds are consistently less than 5%, and that the blowout results are symmetrical to the collapse ones. The comprehensive data can be viewed in Tables 5 and 6. As stated above for the blowout scenario with negative N_c values, the tunnel support pressure σ_t must be larger than the driving pressure $\sigma_s + \gamma H$ (refer to Eq. (1)).

Fig. 7 shows the final 3D adaptive mesh and the associated failure mechanism using the values of shear dissipation, while Figs. 8 and 9 present the 2D views of the side and top views of shear dissipation and velocity contours, respectively, for $H/D = 1$, and $B/D = 1$ and 5. As previously discussed, the produced non-zero shear dissipation values are not representative of such a perfectly plastic material and are therefore not pertinent to the study. Instead, it is essential to focus on the overall presentation of potential shear bands and failure mechanisms (see colored contour plots). It should be noted that the current 3D formulation of FELA provides constant power dissipations using 4-noded tetrahedrons, which may result in some contour discontinuity in Figs. 7 and 8. According to Sloan (2013), this can be improved by using more elements in all analyses and using higher-order elements with quadratic velocity fields. It is noteworthy that repeating Fig. 8, but with the velocity contour plots (nodal values of velocity), has achieved much refined yet smoother failure slip surfaces, as shown in Fig. 9. By inspecting Figs. 7–9, it can be concluded that as B/D increases (i.e. transforming from square to rectangular), the failure extent of ground surface changes from a circle to an ellipse. Furthermore, the overall failure zone increases as B/D increases.

Figs. 10–12 present the corresponding plots for a depth ratio of $H/D = 5$. For $H/D = 10$ in the current study, the three distinct plots

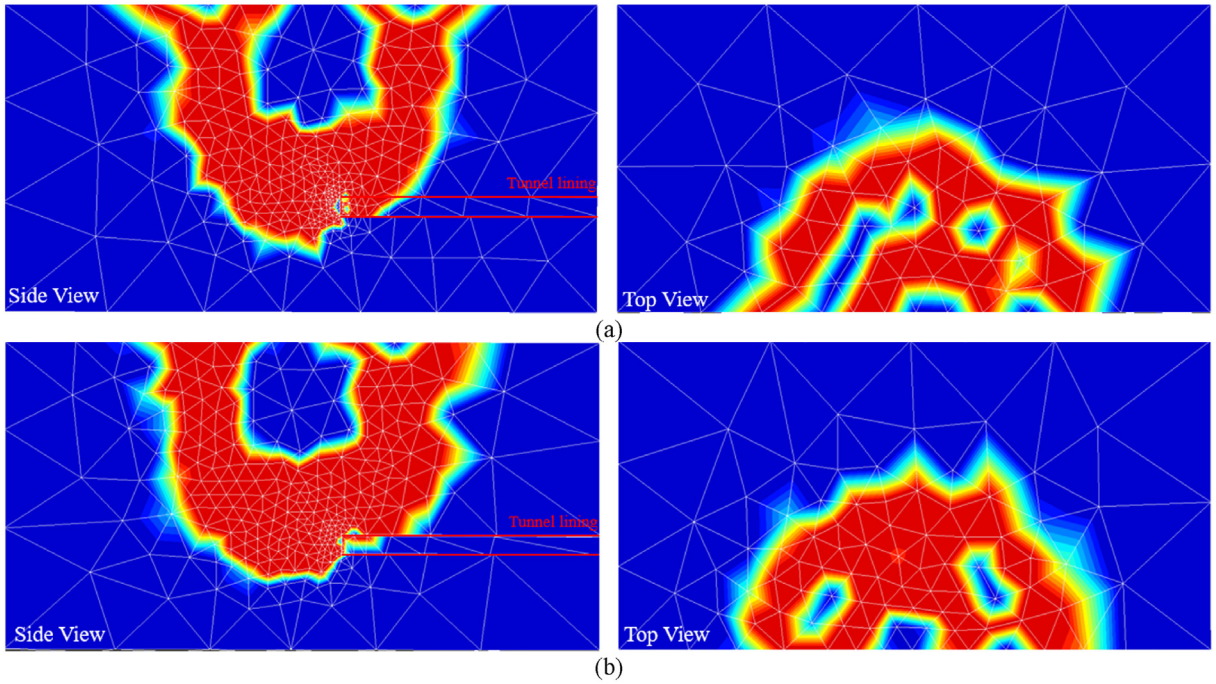

Fig. 14. Side and top views of shear dissipation contour ($H/D = 10$): (a) $B/D = 1$; and (b) $B/D = 5$.

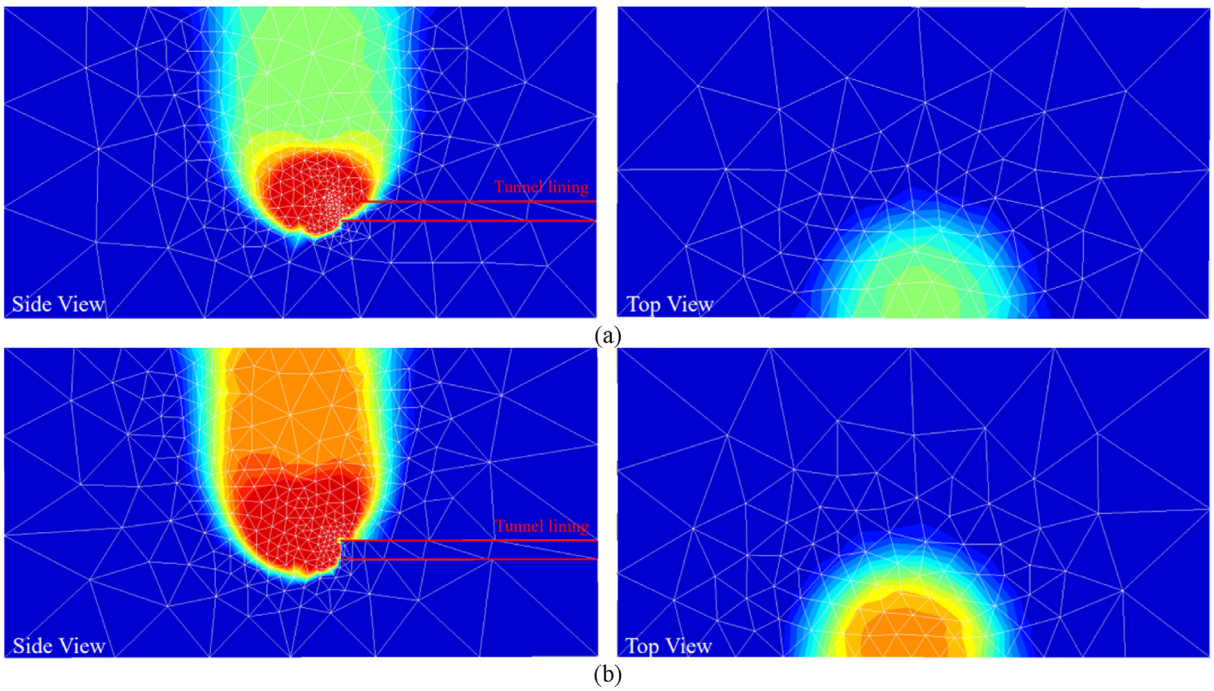

Fig. 15. Side and top views of velocity contour ($H/D = 10$): (a) $B/D = 1$; and (b) $B/D = 5$.

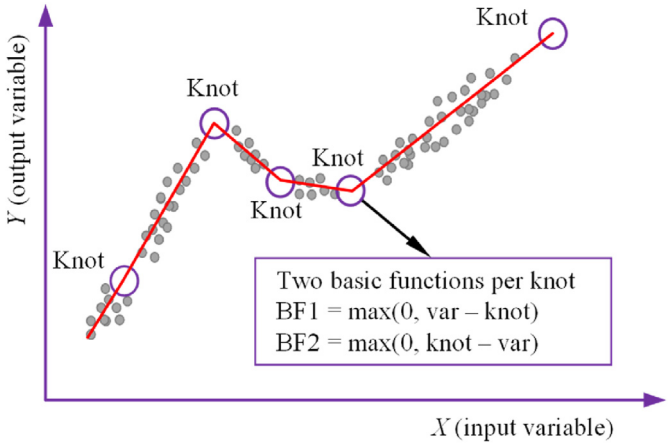

Fig. 16. The concept of MARS model.

are shown in Figs. 13–15. In general, the larger the H/D (depth ratio) and the B/D (width ratio), the greater the failure zone. Nevertheless, one important yet interesting finding for the deep cases ($H/D = 5$ and 10) is that the ellipse-shaped configuration (see Figs. 7–9) resulting from the shallow depth ($H/D = 1$) with large width ratio ($B/D = 5$) no longer persists. In contrast, near-perfect circles are observed in the deeper cases ($H/D = 5$ and 10), despite the large width ratio B/D. This phenomenon is illustrated in Figs. 12 and 15, respectively. The underlying cause can be attributed to the enhanced influence of geometrical and soil arching in deep cases, particularly those with $H/D = 5$ and 10, in comparison to the shallow case of $H/D = 1$.

5. Correlation function and sensitivity study using MARS model

Machine learning has become a popular application in all fields due to its usability in data analysis. In a broader sense, machine learning models can be divided into four categories, i.e. neuron-based (multi-layer perceptron (MLP), generative regression neural network (GRNN), artificial neural network (ANN), and adaptive neuro-fuzzy inference system (ANFIS)), tree-based (M5 model tree (M5Tree) and extreme gradient boosting (XGBoost)), kernel-based (support vector machine (SVM) and KNEA), and curve-based (MARS) models. Recently, it has also been used extensively in geotechnical engineering fields. Published works in the field may include the use of MLP to determine the in situ properties of rock (Miah et al., 2020), the study of bearing capacity of shallow foundations on rock masses using ANN (Millán et al., 2021), the use of ANN, SVM and M5Tree to predict geotechnical parameters (Puri et al., 2018; Wu et al., 2021; Lai et al., 2022a, b; Shiau et al., 2023), and the use of MARS model to analyze deep excavation and caisson foundation (Zhang et al., 2019, 2022; Qureshi et al., 2021). It was generally acknowledged that both the machine learning method and MARS model were effective and efficient (Wu and Fan, 2019; Raja and Shukla, 2021; Lai and Shiau et al., 2023a, b).

The MARS algorithm determines the nonlinear relationship between input and output variables by using a series of piecewise linear functions (splines) with different gradients, as shown conceptually in Fig. 16. For this reason, the MARS model has also been referred to as a curve-based machine learning method (Wu and Fan, 2019). There are two steps in the MARS algorithm. In the first step, the data are divided into several parts. For each part, an individual linear regression model is implemented, and the regression line is generated. The regression lines (splines) are mathematically expressed by several basic functions. Two splines are connected by knots, which are the end of one spline and the start of another spline. Each knot therefore has a pair of basic functions. The first basic function is 'max(0, var − knot)', which means that it takes the maximum value from two options: 0 or the result of the equation 'variable value − value of the knot'. Conversely, the second basic function is 'max (0, knot − var)', as show in Fig. 16. A standard form of the basic functions is presented

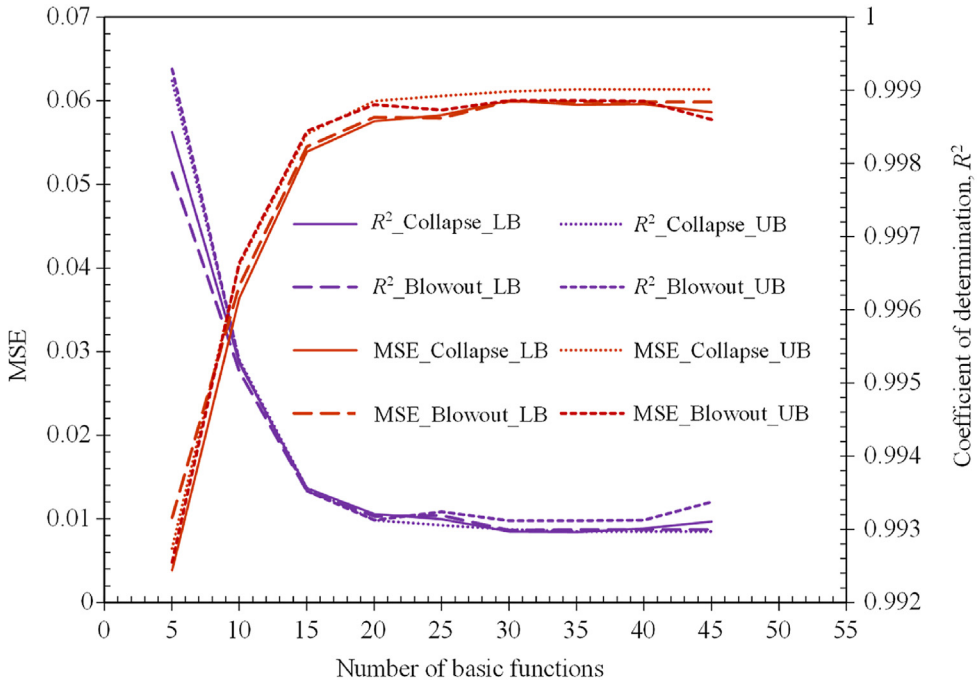

Fig. 17. Effect of the number of basic functions on the performance of predicted MARS models.

Table 7
The basic functions (collapse, LB).

Basic function	Equation	Basic function	Equation
BF 1	$BF1 = \max(0, H/D - 4)$	*BF*21	$BF21 = \max(0, 5 - H/D)$
BF 2	$BF2 = \max(0, 4 - H/D)$	*BF*22	$BF22 = \max(0, B/D - 2)BF21$
BF 3	$BF3 = \max(0, B/D - 2)$	*BF*23	$BF23 = \max(0, 2 - B/D)BF21$
BF 4	$BF4 = \max(0, 2 - B/D)$	*BF*24	$BF24 = \max(0, H/D - 8)$
*BF*5	$BF5 = \max(0, B/D - 1)$	*BF*27	$BF27 = \max(0, 4 - B/D)$
*BF*11	$BF11 = \max(0, H/D - 3)$	*BF*28	$BF28 = \max(0, H/D - 6)$
*BF*16	$BF16 = \max(0, 4 - B/D)BF11$	BF30	$BF30 = \max(0, H/D - 1)BF27$
*BF*18	$BF18 = \max(0, B/D - 3)$		

Table 8
The basic functions (collapse, UB).

Basic function	Equation	Basic function	Equation
*BF*1	$BF1 = \max(0, H/D - 4)$	*BF*16	$BF16 = \max(0, 2 - B/D)BF10$
*BF*2	$BF2 = \max(0, 4 - H/D)$	*BF*20	$BF20 = \max(0, 4 - B/D)$
*BF*3	$BF3 = \max(0, B/D - 2)$	*BF*22	$BF22 = \max(0, 3 - H/D)BF20$
*BF*4	$BF4 = \max(0, 2 - B/D)$	*BF*23	$BF23 = \max(0, H/D - 8)$
*BF*5	$BF5 = \max(0, B/D - 1)$	*BF*25	$BF25 = \max(0, H/D - 6)$
*BF*10	$BF10 = \max(0, 7 - H/D)$	*BF*26	$BF26 = \max(0, 6 - H/D)$
*BF*11	$BF11 = \max(0, H/D - 3)$	*BF*28	$BF28 = \max(0, B/D - 0.5)BF26$
*BF*13	$BF13 = \max(0, B/D - 3)$		

Table 9
The basic functions (blowout, LB).

Basic function	Equation	Basic function	Equation
*BF*1	$BF1 = \max(0, H/D - 4)$	*BF*17	$BF17 = \max(0, H/D - 1)$BF5
*BF*2	$BF2 = \max(0, 4 - H/D)$	*BF*18	$BF18 = \max(0, B/D - 3)$
*BF*3	$BF3 = \max(0, B/D - 2)$	*BF*20	$BF20 = \max(0, H/D - 5)$
*BF*4	$BF4 = \max(0, 2 - B/D)$	*BF*21	$BF21 = \max(0, 5 - H/D)$
*BF*5	$BF5 = \max(0, B/D - 1)$	*BF*23	$BF23 = \max(0, 2 - B/D)BF21$
*BF*9	$BF9 = \max(0, H/D - 7)$	*BF*27	$BF27 = \max(0, 4 - B/D)$
*BF*11	$BF11 = \max(0, H/D - 3)$	*BF*28	$BF28 = \max(0, H/D - 1)BF27$
*BF*16	$BF16 = \max(0, 4 - B/D)BF11$		

Table 10
The basic functions (blowout, UB).

Basic function	Equation	Basic function	Equation
$BF1$	$BF1 = \max(0, H/D - 4)$	$BF12$	$BF12 = \max(0, 3 - H/D)$
$BF2$	$BF2 = \max(0, 4 - H/D)$	$BF13$	$BF13 = \max(0, B/D - 3)$
$BF3$	$BF3 = \max(0, B/D - 2)$	$BF16$	$BF16 = \max(0, 2 - B/D)BF10$
$BF4$	$BF4 = \max(0, 2 - B/D)$	$BF17$	$BF17 = \max(0, H/D - 6)$
$BF5$	$BF5 = \max(0, B/D - 1)$	$BF18$	$BF18 = \max(0, 6 - H/D)$
$BF10$	$BF10 = \max(0, 7 - H/D)$	$BF19$	$BF19 = \max(0, B/D - 0.5)BF12$
$BF11$	$BF11 = \max(0, H/D - 3)$	$BF27$	$BF27 = \max(0, B/D - 2)BF18$

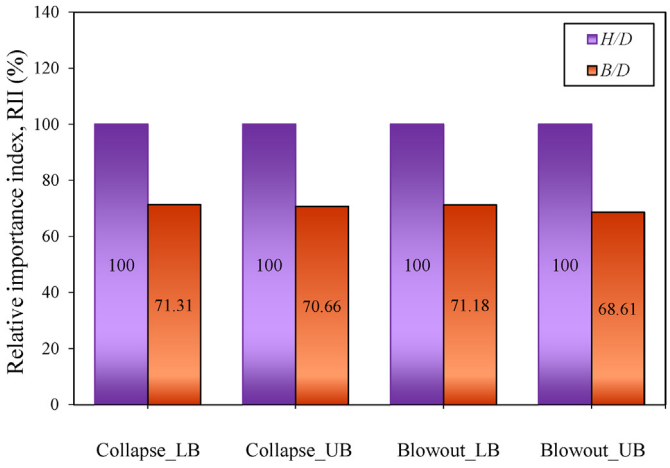

Fig. 18. RII values in different situations.

as follows (Zhang et al., 2019):

$$BF = \max(0, x - t) = \begin{cases} x - t & (x \geq t) \\ 0 & (x < t) \end{cases} \tag{2}$$

where x is an input variable, and t is a knot value. It is noted that the knot position is automatically evaluated using an algorithm with adaptive regression.

In the second step (backward step), the MARS model eliminates the least effective term of the basic functions using the generalized cross validation (GCV) criterion (Friedman, 1991). Consequently, in the final MARS model, the term in question is absent from some basic functions when compared to the initial model.

To mathematically describe the relationship between the input and output variables, the MARS model builds a correlation function by combining all linear basic functions as follows:

$$f(x) = a_0 + \sum_{n=1}^{N} a_n g_n(X) \tag{3}$$

where N is the number of basic functions, a_0 is a constant, g_n is the nth basic function, a_n is the nth coefficient of g_n.

This paper establishes the correlation function between input variables such as B/D and H/D and the output results of stability number (N_c) using the MARS model. The 240 dataset of input variables in Tables 5 and 6 are used as the feeding data for the MARS model. As is well known, increasing the number of basic functions can improve the generalization ability of the MARS model (Wu and Fan, 2019; Raja and Shukla, 2021). To select the best model, the basic function is thus varied while two criteria of statistical analysis, namely mean squared error (MSE) and coefficient of determination (R^2), are adopted to examine the performance of the MARS models. As illustrated in Fig. 17, the MSE values of the MARS models decrease sharply while R^2 values increase dramatically as the number of basic functions increases from 5 to 20, after which they converge to a constant value that approaches the final solution. Notably, the MSE values are the smallest and R^2 values are the largest when the number of basic functions is 30. Consequently, the MARS models with 30 basic functions were selected as the optimal prediction model for constructing the correlation functions.

Tables 7–10 show the best correlation functions with their basic functions using the MARS models. The equations of the correlation functions are respectively shown as follows:

$$\begin{aligned} N_{c-collapse}^{LB} = {} & 8.59149 + 1.18816BF1 - 1.44196BF2 - 1.96502BF3 \\ & + 2.43552BF4 \\ & + 1.27293BF5 - 0.418585BF11 - 0.111846BF16 \\ & + 0.242243BF18 + 0.0439862BF22 \\ & + 0.0752542BF23 - 0.130238BF24 - 0.238231BF28 \\ & + 0.0980762BF30 \end{aligned} \tag{4}$$

$$\begin{aligned} N_{c-collapse}^{UB} = {} & 9.19532 + 1.38278BF1 - 1.55772BF2 - 2.37371BF3 \\ & + 2.83932BF4 + 1.46992BF5 - 0.492537BF11 + 0.357988BF13 \\ & + 0.0840612BF16 - 0.0959836BF22 - 0.126646BF23 \\ & - 0.319227BF25 + 0.0338063BF28 \end{aligned} \tag{5}$$

$$\begin{aligned} N_{c-blowout}^{LB} = {} & -8.49439 - 1.30182BF1 + 1.41186BF2 \\ & + 1.8239BF3 - 2.35781BF4 - 1.29924BF5 + 0.176048BF9 \\ & + 0.378776BF11 + 0.155698BF16 \\ & + 0.02749BF17 - 0.238063BF18 \\ & + 0.222552BF20 - 0.0900482BF23 - 0.125033BF28 \end{aligned} \tag{6}$$

$$\begin{aligned} N_{c-blowout}^{UB} = {} & -9.61282 - 1.69495BF1 + 1.83596BF2 \\ & + 2.40325BF3 - 2.90509BF4 - 1.50941BF5 \\ & + 0.837863BF11 - 0.351424BF13 - 0.0464434BF16 \\ & + 0.356066BF17 - 0.0902603BF19 - 0.0256582BF27 \end{aligned} \tag{7}$$

In addition to establishing Eqs. (4)–(7), the MARS models can also be used to investigate the sensitivity of input variables to the output results. This is represented by the relative importance index (RII, in %) in Fig. 18. A value of 100% for the RII indicates that the variable in question is the most influential in determining the value of N. As shown in Fig. 18, H/D is the most important design variable (with the RII value of 100%), followed by B/D with an RII value of 70%.

A comparison between the stability number determined from

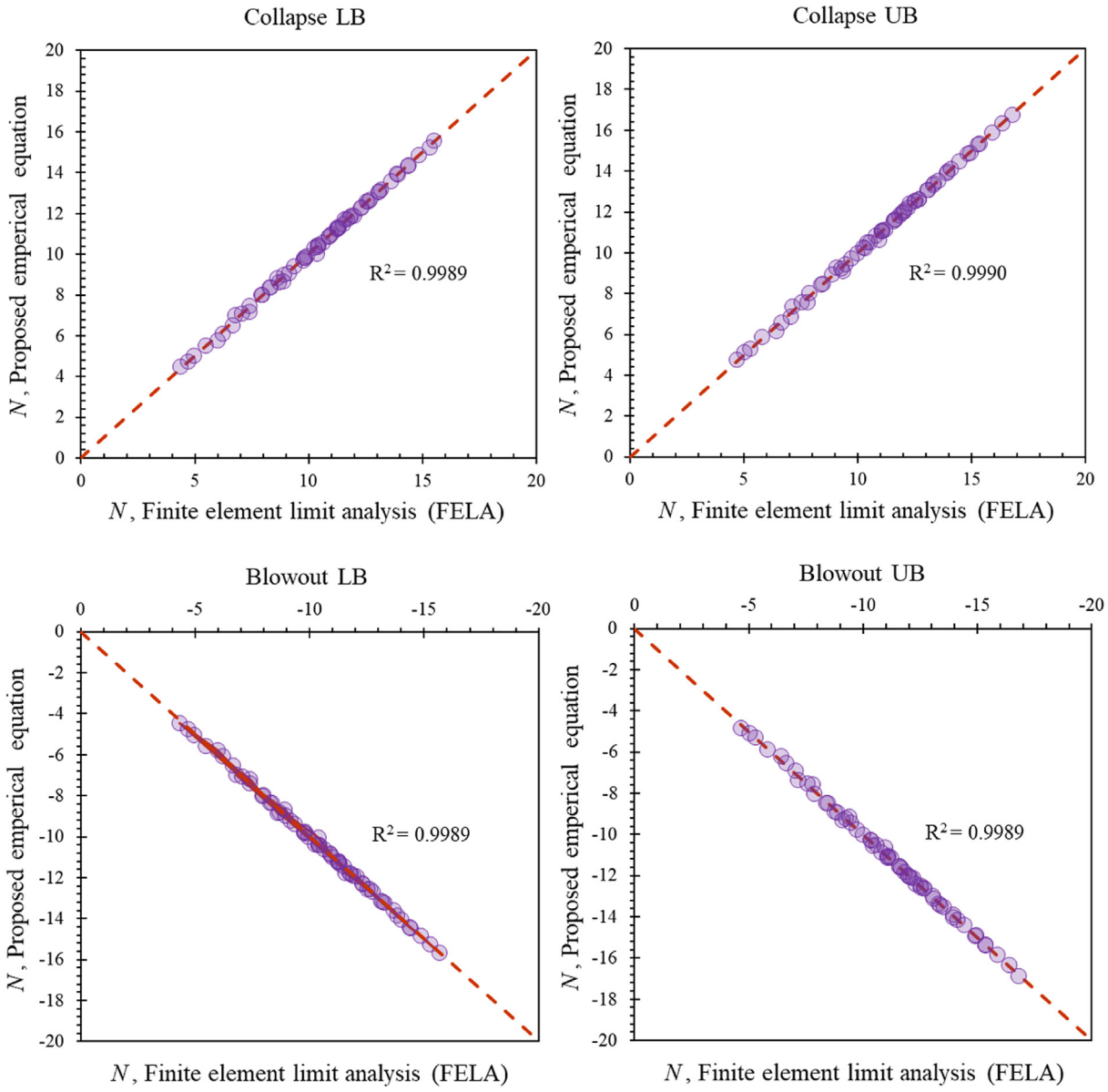

Fig. 19. Comparison of the stability number (N) results between proposed empirical equations and FELA.

FELA and the correlation functions is shown in Fig. 19. The excellent fit between Eqs. (4)–(7) and those from FELA analyses, as well as the values of R^2, allows the conclusion to be drawn that the proposed functions can be confidently used to predict critical stability numbers of rectangular tunnel headings in undrained condition for cohesive soils.

Another comparison with those experimental results of 3D circular tunnels by Kimura and Mair (1981) is presented in Fig. 20. The results demonstrate a good agreement with our current machine learning predictions, exhibiting an average discrepancy of 10%–15% relative to the experimental results. The comparisons presented in Figs. 19 and 20 have successfully validated the reliability of the produced results in this paper.

6. Factor of safety

Shiau and Al-Asadi (2018, 2020) conducted several undrained stability studies on the relationship between the FoS and N in subterranean tunneling stability. It was concluded that the FoS and the 'designed' N values have a hyperbolic correlation, which can be stated as

$$FoS = \frac{N_c}{N} \tag{8}$$

As $FoS = 1$, the stability number N is equal to the critical N_c

The following equations can be used to compute the FOS for the 3D rectangular tunnel while considering the overall influence of H/D and B/D on the stability number N:

$$FoS^{LB}_{collapse} = N^{LB}_{c-collapse} \Big/ N \tag{9}$$

$$FoS^{UB}_{collapse} = N^{UB}_{c-collapse} \Big/ N \tag{10}$$

Similarly, the blowout FoS can be evaluated as follows:

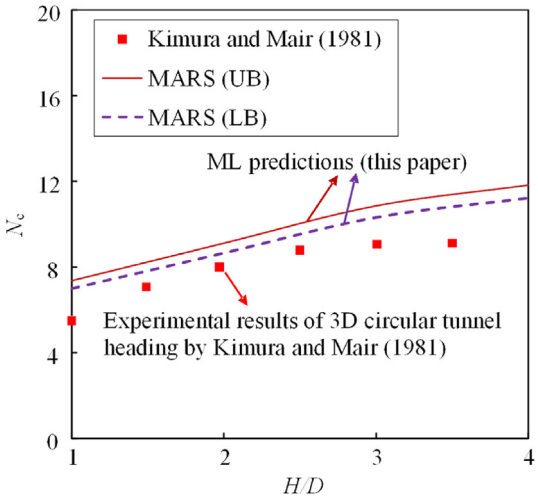

Fig. 20. Comparison of N_c results between proposed empirical equation and 3D experimental results.

$$FoS^{LB}_{blowout} = N^{LB}_{c-blowout} \Big/ N \tag{11}$$

$$FoS^{UB}_{blowout} = N^{UB}_{c-blowout} \Big/ N \tag{12}$$

Fig. 21 presents a set of 3D FoS data and illustrates the asymptotic relationship between N and FoS according to Eqs. (9)–(12), where $B/D = 1$, and $H/D = 1$ and 10. The negative sign of N indicates a blowout condition, while the collapse condition has positive values of N. If a horizontal line is drawn at $FoS = 1$, the four intersection points indicate the corresponding critical values of N_c where the associated $FoS = 1$. It should be noted that the FoS value decreases as the absolute values of N increases in both collapse and blowout situations. In the collapse condition, an increase in N indicates an increase in overburden pressure ($\sigma_s + \gamma H$), which consequently results in a decrease in the FoS.

For $H/D = 1$, and $B/D = 1$ and 5, the relationship between the FoS

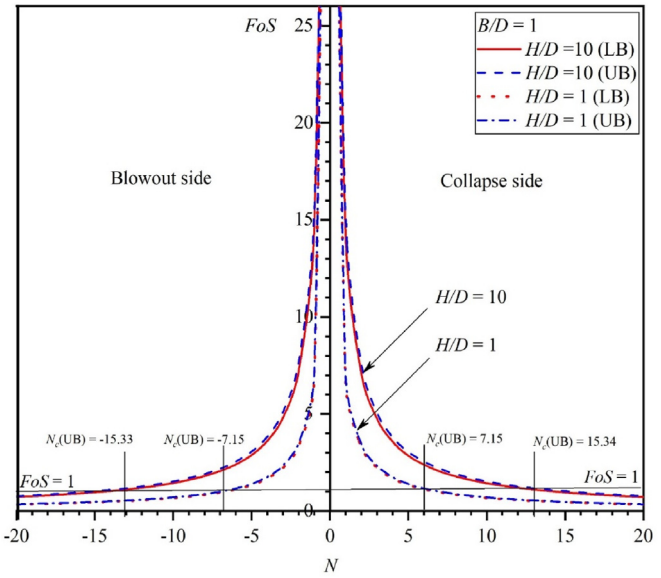

Fig. 21. N vs. FoS relations ($B/D = 1$).

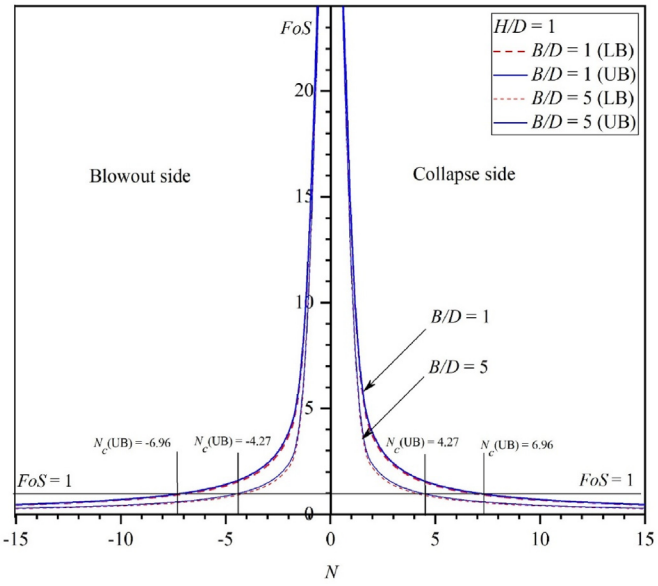

Fig. 22. N vs. FoS relations ($H/D = 1$).

and N is shown in Fig. 22. A similar observation can be made as shown in Fig. 20. It is important to note that, for a given value of N, $B/D = 1$ produces a greater FoS value than $B/D = 5$. Indeed, a square tunnel is more stable than a rectangular one. Since the FoS has been well known and widely used by practical engineers, the FoS equations provided would assist practical engineers in their early design stages.

7. Conclusions

Using the novel UB and LB FELAs, this paper has effectively investigated the stability of 3D rectangular tunnel headings for a range of different design parameters in both blowout and collapse conditions. The numerical output of dimensionless stability numbers has been used as training data for the MARS analysis, leading to the development of a number of design equations. The following conclusions are drawn from the study of this paper.

(1) The value of the critical stability number N_c on the collapse side has a positive sign. A negative value of N_c would represent a blowout condition. The results of both the collapse and blowout situations are symmetrical.

(2) By comparing the 3D square heading results with the 3D circular heading results, it was found that the N_c results of the square tunnel heading were approximately 1% less than those of the 3D circular heading. It was therefore concluded that the 3D circular tunnel heading is more stable than the square tunnel ($B/D = 1$).

(3) The N_c results of the 3D square heading were compared to those of 2D plane-strain tunnel headings ($B/D = \infty$) for both the blowout and collapse conditions. In general, depending on the value of B/D, the 3D analysis predicts larger values of N_c by approximately 1.7–1.9 times. The presented design margin between 2D and 3D analyses provides useful information for the stability assessment of 3D rectangular tunnel heading for $B/D > 1$.

(4) Numerical results of shear power dissipation have shown that as the width ratio B/D increases (from square to rectangular), the failure extent of the ground surface changes from a circular to an elliptical shape. As the depth ratio H/D

increases, owing to the stronger effect of geometrical and soil arching, all the ground surfaces fail in circular shapes.

(5) Accurate design equations have been successfully developed using the MARS analysis, and an equation for calculating the FoS has also been proposed. These equations can be confidently used by design practitioners.

The current FELA model considers a homogeneous and isotropic soil. It is recommended that future work be directed towards more realistic situations such as multiple soil layers and anisotropic conditions.

Declaration of competing interest

The authors declare that they have no known competing financial interests or personal relationships that could have appeared to influence the work reported in this paper.

Acknowledgments

This work was supported by the Thailand Science Research and Innovation Fundamental Fund fiscal year 2023. The fifth author (V. Kamchoom) acknowledges the financial support from the National Science, Research and Innovation Fund (NSRF) at King Mongkut's Institute of Technology Ladkrabang (KMITL), Thailand (Grant No. FRB66065/0258-RE-KRIS/FF66/53), the Climate Change and Climate Variability Research in Monsoon Asia (CMON3) from the National Research Council of Thailand (NRCT) (Grant No. N10A650844), and the National Natural Science Foundation of China (NSFC). We also acknowledge Ho Chi Minh City University of Technology (HCMUT) and VNU-HCM for supporting this study.

Appendix A. Supplementary data

Supplementary data to this article can be found online at https://doi.org/10.1016/j.jrmge.2023.12.035.

References

Abbo, A.J., Wilson, D.W., Sloan, S.W., Lyamin, A.V., 2013. Undrained stability of wide rectangular tunnels. Comput. Geotech. 53, 46–59.
Assadi, A., Sloan, S.W., 1991. Undrained stability of shallow square tunnel. J. Geotech. Eng. 117 (8), 1152–1173.
Broms, B.B., Bennermark, H., 1967. Stability of clay at vertical openings. J. Soil Mech. Found. Div. ASCE 93, 71–94.
Chambon, P., Corté, J.F., 1994. Shallow tunnels in cohesionless soil: stability of tunnel face. J. Geotech. Eng. 120 (7), 1148–1165.
Dutta, P., Bhattacharya, P., 2021. Stability of rectangular tunnel in cohesionless soils. Int. J. Geotech. Eng. 15 (10), 1345–1351.
Friedman, J.H., 1991. Multivariate adaptive regression splines. Ann. Stat. 19, 1–67.
Keawsawasvong, S., Shiau, J., 2022. Stability of active trapdoors in axisymmetry. Undergr. Space 7 (1), 50–57.
Keawsawasvong, S., Ukritchon, B., 2019. Undrained stability of a spherical cavity in cohesive soils using finite element limit analysis. J. Rock Mech. Geotech. Eng. 11 (6), 1274–1285.
Kimura, T., Mair, R.J., 1981. Centrifuge testing of model tunnels in soft clays. In: In: Proceedings of the 10th International Conference on Soil Mechanics and Foundation Engineering, vol. 1. International Society for Soil Mechanics and Foundation, London, UK, pp. 319–322.
Lai, V.Q., Lai, F., Yang, D., Shiau, J., Yodsomjai, W., Keawsawasvong, S., 2022a. Determining seismic bearing capacity of footings embedded in cohesive soil slopes using multivariate adaptive regression splines. Int. J. Geosynth. Ground Eng. 8, 46.
Lai, V.Q., Shiau, J., Keawsawasvong, S., Tran, D.T., 2022b. Bearing capacity of ring foundations on anisotropic and heterogenous clays: FEA, NGI-ADP, and MARS. Geotech. Geol. Eng. 40, 3929–3941.
Lai, V.Q., Shiau, J., Promwichai, T., Limkatanyu, S., Banyong, R., Keawsawasvong, S., 2023a. Modelling soil stability in wide tunnels using FELA and multivariate adaptive regression splines analysis. Model. Earth Syst. Environ. 9, 2993–3008.
Lai, F., Shiau, J., Keawsawasvong, S., Chen, F., Banyong, R., Seehavong, S., 2023b. Physics-based and data-driven modeling for stability evaluation of buried structures in natural clays. J. Rock Mech. Geotech. Eng. 15 (5), 1248–1262.
Leca, E., Dormieux, L., 1990. Upper and lower bound solutions for the face stability of shallow circular tunnels in frictional material. Geotechnique 40 (4), 581–606.
Man, J., Zhou, M., Zhang, D., Huang, H., Chen, J., 2022. Face stability analysis of circular tunnels in layered rock masses using the upper bound theorem. J. Rock Mech. Geotech. Eng. 14 (6), 1836–1848.
Miah, M.I., Ahmed, S., Zendehboudi, S., Butt, S., 2020. Machine learning approach to model rock strength: prediction and variable selection with aid of log data. Rock Mech. Rock Eng. 53 (10), 4691–4715.
Millán, M.A., Galindo, R., Alencar, A., 2021. Application of artificial neural networks for predicting the bearing capacity of shallow foundations on rock masses. Rock Mech. Rock Eng. 54, 5071–5094.
Mollon, G., Dias, D., Soubra, A.H., 2010. Face stability analysis of circular tunnels driven by a pressurized shield. J. Geotech. Geoenviron. Eng. 136 (1), 215–229.
Mühlhaus, H.B., 1985. Lower bound solutions for circular tunnels in two and three dimensions. Rock Mech. Rock Eng. 18 (1), 37–52.
Puri, N., Prasad, H.D., Jain, A., 2018. Prediction of geotechnical parameters using machine learning techniques. Procedia Comput. Sci. 125, 509–517.
Qureshi, M.U., Mahmood, Z., Rasool, A.M., 2021. Using multivariate adaptive regression splines to develop relationship between rock quality designation and permeability. J. Rock Mech. Geotech. Eng. 14 (4), 1180–1187.
Raja, M.N.A., Shukla, S.K., 2021. Multivariate adaptive regression splines model for reinforced soil foundations. Geosynth. Int. 28, 368–390.
Sahoo, J.P., Kumar, J., 2014. Stability of a circular tunnel in presence of pseudostatic seismic body forces. Tunn. Undergr. Space Technol. 42, 264–276.
Shiau, J., Al-Asadi, F., 2018. Revisiting Broms and Bennermarks' original stability number for tunnel headings. Géotech. Lett. 8 (4), 310–315.
Shiau, J., Sams, M., 2019. Relating volume loss and greenfield settlement. Tunn. Undergr. Space Technol. 83, 145–152.
Shiau, J., Al-Asadi, F., 2020. Three-dimensional analysis of circular tunnel headings using Broms and Bennermark's original stability number. Int. J. GeoMech. 20 (7). https://doi.org/10.1061/(ASCE)GM.1943-5622.000173.
Shiau, J., Keawsawasvong, S., Chudal, B., Mahalingasivam, K., Seehavong, S., 2021a. Sinkhole stability in elliptical cavity under collapse and blowout conditions. Geosciences 11 (10), 421.
Shiau, J., Lee, J.S., Al-Asadi, F., 2021b. Three-dimensional stability analysis of active and passive trapdoors. Tunn. Undergr. Space Technol. 107, 103635.
Shiau, J., Keawsawasvong, S., 2022. Producing undrained stability factors for various tunnel shapes. Int. J. GeoMech. 22 (8), 06022017.
Shiau, J., Lai, V.Q., Keawsawasvong, S., 2023. Multivariate adaptive regression splines analysis for three-dimensional slope stability in anisotropic and heterogenous clay. J. Rock Mech. Geotech. Eng. 15 (4), 1052–1064.
Sloan, S.W., 2013. Geotechnical stability analysis. Geotechnique 63 (7), 531–572.
Sloan, S.W., Assadi, A., 1993. Stability of shallow tunnels in soft Ground. In: Holsby, G.T., Schofield, A.N. (Eds.), Predictive Soil Mechanics. Thomas Telford, London, UK, pp. 644–663.
Ukritchon, B., Keawsawasvong, S., 2018. A new design equation for drained stability of conical slopes in cohesive-frictional soils. J. Rock Mech. Geotech. Eng. 10 (2), 358–366.
Wilson, D.W., Abbo, A.J., Sloan, S.W., Lyamin, A.V., 2013. Undrained stability of a square tunnel where the shear strength increases linearly with depth. Comput. Geotech. 49, 314–325.
Wu, L., Fan, J., 2019. Comparison of neuron-based, kernel-based, tree-based and curve-based machine learning models for predicting daily reference evapotranspiration. PLoS One 14, e0217520.
Wu, Z., Wei, R., Chu, Z., Liu, Q., 2021. Real-time rock mass condition prediction with TBM tunneling big data using a novel rock–machine mutual feedback perception method. J. Rock Mech. Geotech. Eng. 13 (6), 1311–1325.
Zhang, W., Zhang, R., Wang, W., Zhang, F., Goh, A.T.C., 2019. A multivariate adaptive regression splines model for determining horizontal wall deflection envelope for braced excavations in clays. Tunn. Undergr. Space Technol. 84, 461–471.
Zhang, W., Li, H., Han, L., Chen, L., Wang, L., 2022. Slope stability prediction using ensemble learning techniques: a case study in Yunyang County, Chongqing, China. J. Rock Mech. Geotech. Eng. 14 (4), 1089–1099.

Jim Shiau is currently Associate Professor at University of Southern Queensland, Australia. He received a PhD degree from University of Newcastle, NSW, Australia, where he continued two years of post-doctorate under the leadership of late Laureate Professor Scott Sloan. His research focuses on deep braced excavation and soft ground tunneling, sinkhole stability, and finite element limit and shakedown analyses for geotechnical stability problems. Shiau has extensive experience in the design of underground structures. He enjoys the breadth of general practice with interests in geotechnical stability research. He has published more than 20 high-impact Q1 journal articles as being both first and corresponding authors. Dr. Shiau is a passionate and creative educator in geotechnical engineering. He is experienced in geotechnical education with the uses of project-based learning, physical modeling, and short videos for online learning. He was a winner of the USQ Teaching Award.